

Compact Nested Hexagonal Metamaterial Sensor for High-Sensitivity Permittivity Characterization Across S and X-Band Frequencies

¹Md Mujahid Hossain, ¹Saif Hannan

¹Department of Electronic and Telecommunication Engineering, International Islamic University Chittagong (IIUC), Chattogram 4318, Bangladesh

Abstract

This article presents a Compact Nested Hexagonal Metamaterial Sensor designed for microwave sensing to characterize material permittivity in S and X-band applications. The proposed sensor attained compact dimensions of merely 30 mm x 30 mm x 0.79 mm. This innovative design technique employs a distinctive and compact architecture with elevated electromagnetic (EM) field strength, enhancing the precision of the sensing mechanism in the microwave frequency spectrum. The design geometry and dimensions attained resonance frequencies of 3.98 GHz and 11.57 GHz, with notch depths of -13.16129 dB and -10.23024 dB, respectively. The design evolution, metamaterial properties, equivalent circuit model, and electric (E) is delineated to elucidate the stopband features at the resonant frequency. The suggested sensor attains a very high sensitivity of 9.55% in transmission mode (S_{21}) for a permittivity range of 1 to 6. The reflection and transmission properties of the proposed CRR-based sensor are validated by simulations using the mathematical equations of the design. Furthermore, the sensor's performance is corroborated by utilizing several dielectric materials (Roger R04350B, Roger RT5880 and FR-4). The computed outcomes demonstrate alignment with the simulated results. The compact, low-profile sensor design and its excellent sensitivity for characterizing material permittivity render the suggested sensor appropriate for permittivity sensing applications.

1. Introduction

Microwave-based sensors are essential instruments for sophisticated material characterization, with widespread applications in biosensing, food quality assessment, and the optimization of electromagnetic systems [1]. Their capability to accurately measure dielectric and magnetic properties has generated interest in improving compactness, sensitivity, and precision design [2],[3]. The rising demand for tailored sensors for specific applications has led to recent breakthroughs in metamaterial-based designs, such as split-ring resonators (SRRs), facilitating enhanced performance measures [4].

Much effort has gone into improving permittivity, a critical feature of dielectric materials [5]. It is significant in determining how electromagnetic (EM) waves behave when propagating through microwave system substrate materials [6],[7]. The practical implications of this research are significant, particularly in the context of reducing delays in propagation and parasitic capacitance effects in low-permittivity materials, with a growing demand for creative solutions [8]. Due to their variable permittivity caused by the production process, these low-permittivity materials, typically composites, necessitate accurate measurement. To develop exact electrical systems, perfect permittivity measurement is foundational, not merely a technical necessity [9].

Nevertheless, low-dielectric material permittivity measurements provide distinct difficulties, such as diminished environmental sensitivity and vulnerability. In response to these problems, several measurement techniques based on resonance have been developed, such as free space, microstrip lines, and resonance cavities [10],[11]. To find the MUT's permittivity, one standard method is to use microwave characterization techniques [12]. The microstrip line approach is the mainstay of these techniques [13]. Compared to optical fiber sensors, microwave microstrip sensors have several benefits, including lower production costs and easier manufacturing. This becomes especially clear when compared to biosensors based on fiber-optic localized surface plasmon resonance (LSPR) or fiber Bragg grating (FBG).

Metamaterial structures, such as complementary split-ring resonators (CSRR), split-ring resonators (SRR), magnetic-LC (MLC), and electric-LC (ELC), are frequently integrated into microstrip sensor designs. These structures play a pivotal role in achieving resonance peaks and enhancing the sensing area, thereby significantly improving sensor performance [7,17–26]. A sensor based on symmetrical split-ring resonators is a prime example of this approach, demonstrating enhanced permittivity characterization performance.

A recent study underscores substantial advancements in the development of sensor technologies. Symmetrical SRRs enhanced with spurlines have demonstrated elevated quality (Q) factors and remarkable sensitivity for detecting solid materials [1]. Likewise, SRR-integrated microstrip line designs have enabled the concurrent measurement of magnetodielectric characteristics, yielding dependable assessments of permeability and permittivity [2]. Innovative topologies, like backbone-shaped resonators, have enhanced sensor capabilities by amplifying electric fields in the detecting regions, attaining sensitivities of up to 6.61% in reflection mode [4]. Notwithstanding these gains, reconciling compactness, sensitivity, and operational adaptability presents problems. This study addresses this deficiency by presenting a Compact Nested Hexagonal Microwave Metamaterial Sensor designed for high-sensitivity permittivity characterization in the S and X-band.

This study posits that the proposed nested hexagonal resonator design, incorporating concentric hexagonal and rectangular structures, significantly enhances electric field confinement, thereby improving sensor sensitivity. Integrating these advanced structural configurations has the potential to outperform traditional designs in precision and versatility, particularly across a range of permittivity values. This potential for superior performance is an exciting prospect for the field of sensor technology.

The study utilizes a stringent methodological framework that integrates computational modeling and experimental validation to assess the proposed sensor's efficacy thoroughly. The sensor design is simulated in CST Microwave Studio to evaluate reflection (S11) and transmission (S21) coefficients, electric field distribution, and resonance characteristics. Experimental validations are performed using typical dielectric materials to confirm the simulation results. This dual method guarantees a comprehensive and rigorous assessment of the sensor's capabilities, encompassing theoretical and practical performance metrics, reinforcing the results' credibility.

Preliminary findings suggest that the proposed sensor markedly improves sensitivity and compactness. The design of the nested hexagonal and rectangular resonator efficiently enhances the electric field intensity in the sensing area, facilitating accurate permittivity measurements. The sensor's small size and great sensitivity render it appropriate for applications necessitating precise material characterization in limited spatial settings. This research advances the field of metamaterial sensors by creating a detailed design framework that overcomes significant constraints in current technology, facilitating potential applications.

The rest of the paper is organized as follows: Section 2 comprehensively analyzes the proposed metamaterial sensor design, including sensor design evolution and electric field and surface current distribution. Section 3 focuses on the sensing result analysis, discussing the sensor's interaction with materials under test (MUT). Section 4 introduces the mathematical modeling of the simulated results, emphasizing polynomial equations to describe the sensor's response. Section 5 compares the proposed sensor with existing designs, highlighting its advantages in terms of compactness and sensitivity. Section 6 presents conclusion of the paper with a summary of key contributions and directions for future research. Finally, Section 7 lists the references used throughout the study.

2. Design and analysis of metamaterial sensors

Design of the sensor

Figure 1 shows the proposed metamaterial sensor called a Compact Nested Hexagonal Shape Resonator in the act. It has three resonators: two stacked hexagonal rings and one rectangular ring. These are all designed to sit on the transmission line, and on the other side of the line, there is a complete copper layer. A thickness of 0.79 mm, a dielectric constant of 2.2, and a loss tangent of 0.0009 characterize the Rogers RT5880 substrate material.

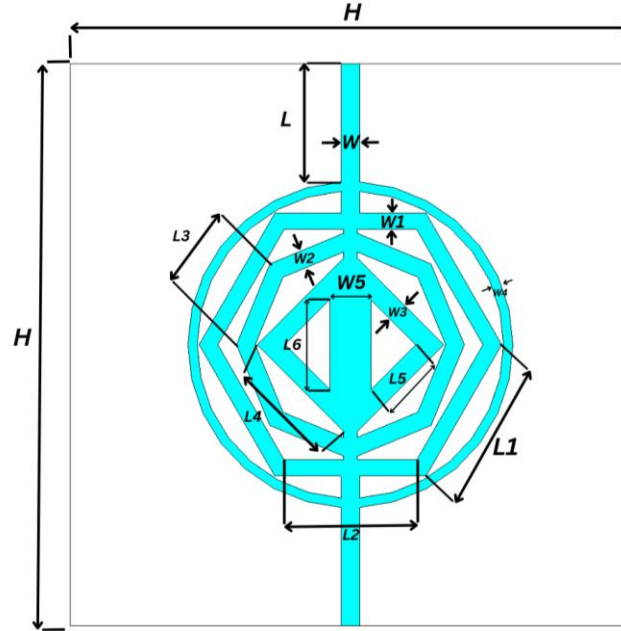


Figure 1. Frontal perspective of the proposed sensor.

The CST microwave application has been used to build and simulate the proposed sensor. Table 1 presents the projected sensor design parameters, while Figure 2 illustrates the reflection coefficients (S_{11}) and transmission (S_{21}) coefficients of the projected metamaterial sensor. The S_{21} parameter exhibits peak resonance frequencies at 3.96 GHz and 11.57 GHz, containing the values of -13.16129 dB and -10.23024 dB, respectively. The peak resonance frequencies of S_{11} are observed at 4.11, 4.16, 5.95, and 10.52 GHz, with corresponding notch depths of -19.78626, -21.769, -41.91938, and -33.70582 dB, respectively. The equivalent circuit model (ECM) illustrated in Figure 3(a) is a high-frequency network constructed with parallel and series RLC components. The model was developed and simulated using the powerful ADS software, a crucial step in assessing the S_{21} parameter that represents the forward transmission characteristics. The circuit, comprising resistors, capacitors, and inductors, is arranged to measure the frequency-dependent impedance and resonance effects, with the ADS software playing a significant role in this process. Figure 3(b) presents a plot of the S_{21} parameter versus frequency. The dashed red line indicates the results from the ADS simulation, while the solid black line represents experimental data or alternative simulation results. The results indicate a strong correlation, with the ADS simulation effectively reflecting the main trends of the frequency response. Peaks and dips in the S_{21} curve indicate resonance effects resulting from the RLC elements present in the model. Discrepancies observed at specific frequencies may be due to parasitic elements or the limitations inherent in the simplifications of the ECM. This analysis not only confirms the applicability of the ECM in RF and microwave circuit designs but also provides valuable insights for future research and practical applications.

Table 1. Design Specifications of the sensor design.

Label	H	L1	L	L2	L3	L4	L5	L6	W	W1	W2	W3	W4	W5
-------	---	----	---	----	----	----	----	----	---	----	----	----	----	----

Dimension (mm)	30.00	8.10	6.31	7.10	4.67	6.56	3.39	4.80	1.00	1.00	1.00	1.50	0.50	2.20
----------------	-------	------	------	------	------	------	------	------	------	------	------	------	------	------

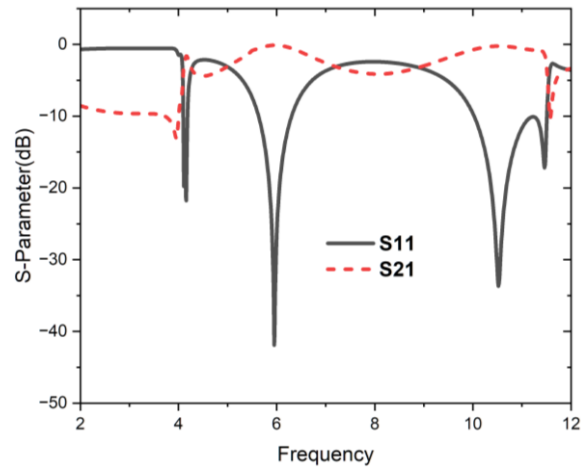


Figure 2. The simulated S_{11} and S_{21} parameters of the proposed sensor are presented.

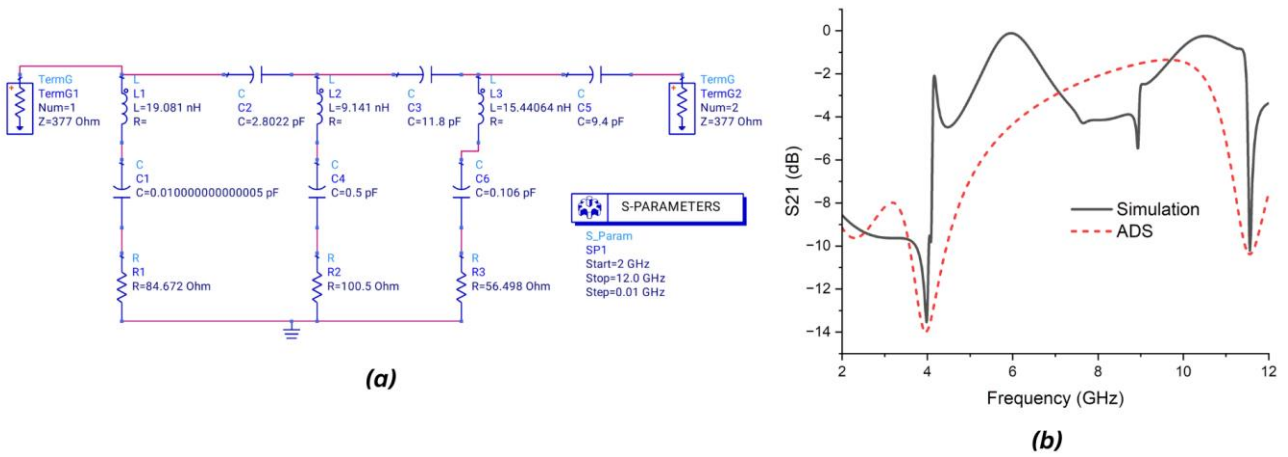
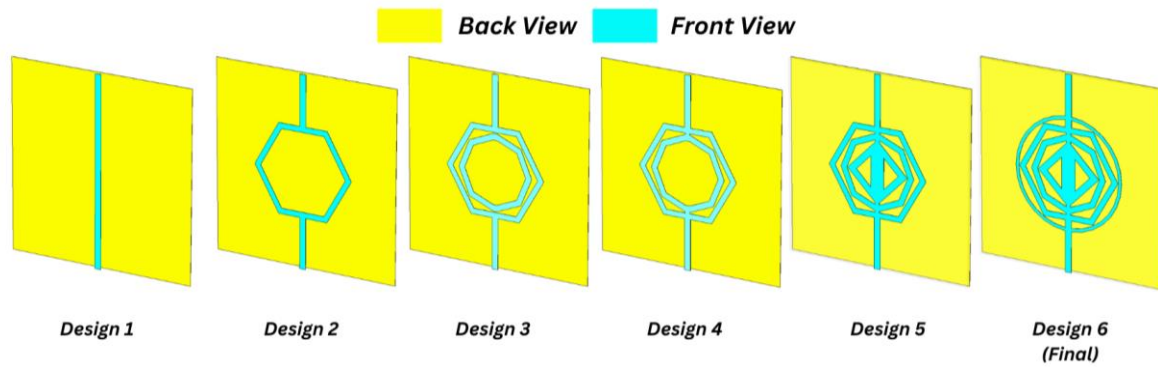


Figure 3. S_{21} circuit simulation results of the proposed sensor using ADS.

Design Evolution

Figure 4 depicts the evolution of the metamaterial, demonstrating a systematic progression through six distinct designs, each playing a role in improving resonance characteristics, as indicated by the S_{11} and S_{21} parameters.



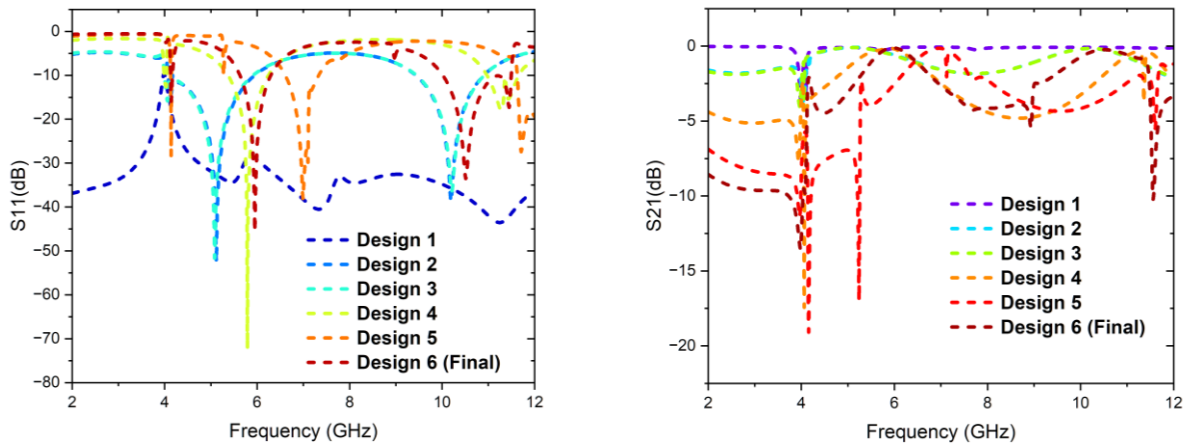


Figure 4. The S_{11} and S_{21} parameters corresponding to various design stages of the proposed sensor.

Design 1 features a straightforward split transmission line structure, which acts as the initial configuration and does not exhibit notable resonance effects within the specified frequency range. Design 2, featuring a single hexagonal ring, represents the initial phase of interaction with electromagnetic waves, as evidenced by a slight dip in the S_{11} (Reflection) graph and negligible variation in the S_{21} (Transmission) response. Design 3, with the addition of an inner octagonal ring, leaps forward, introducing a stopband resonance at a lower frequency, as evidenced by a deeper S_{11} dip and a developing S_{21} resonance. Design 4 represents a critical advancement in the development process, establishing connections between the inner and outer hexagonal and octagonal rings. This configuration enhances coupling, leads to a more distinct resonance in the S_{11} parameter, and achieves a peak in S_{21} at 4.1GHz with a measurement of -11.33dB.

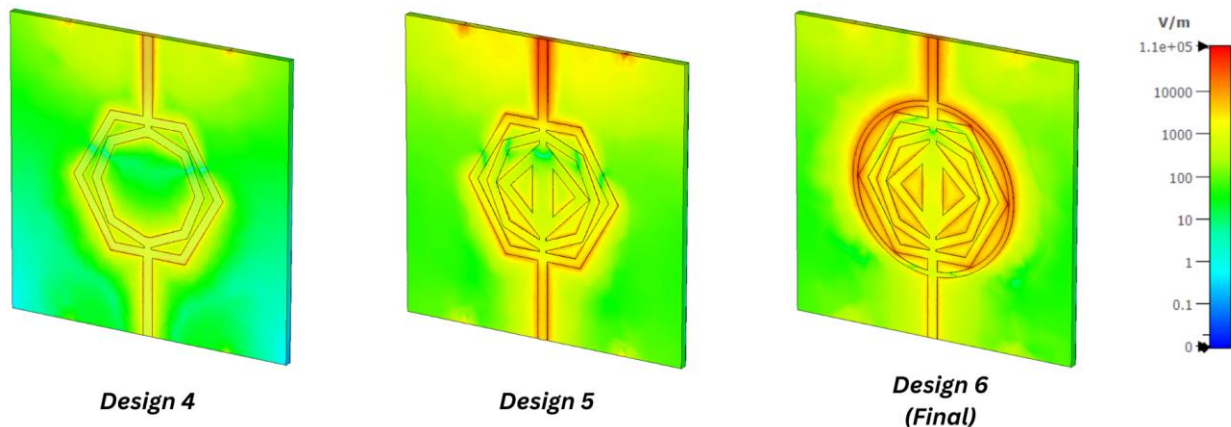


Figure 5. Electric field of the proposed sensor at various design stages.

To ensure a thorough understanding of the sensor's mechanics, we have conducted an analysis of the proposed sensor's electric field dynamics during various design phases, particularly at its resonance frequencies, as depicted in Figure 4. Our research has revealed that the intensified electric field in the sensing region significantly enhances sensitivity to subtle changes in the material's permittivity. This breakthrough has the potential to catalyze additional progress in sensor technology, sparking excitement for the future of the field. In Design 4, the connection of the hexagonal and octagonal rings creates a pronounced disparity in electric field strength. The maximum intensity is found in the ring's arm, while the core region exhibits a significantly reduced intensity. The intensity increases with the connectivity of the positioned ring resonator at the corners; however, the center shows a decrease in

electric field intensity. The combination of the rectangular nested and circular outer ring structure notably boosts the electric field intensity at the sensor's center, which is specifically designed for the positioning of the testing material.

Field of Electricity and Distribution of Surface Current

The electric field and surface current distribution show the resonance properties of transmission and reflection modes, an interesting and complex aspect of metamaterial constructions. An important practical use is seen in Figure 6, which shows the S_{21} resonance frequency at 3.98 GHz. This frequency range is where the metamaterial sensor construction permits electromagnetic waves to pass through with minimum reflection. Similarly, there are practical ramifications because the resonance frequency in reflection mode (5.95 GHz) is in the range of frequency where the structure of the metamaterial substantially blocks the transmission of electromagnetic waves. The intricate surface current distributions seen in metamaterial structures highlight the intellectual difficulty our expertise in electromagnetics and metamaterials must unravel.

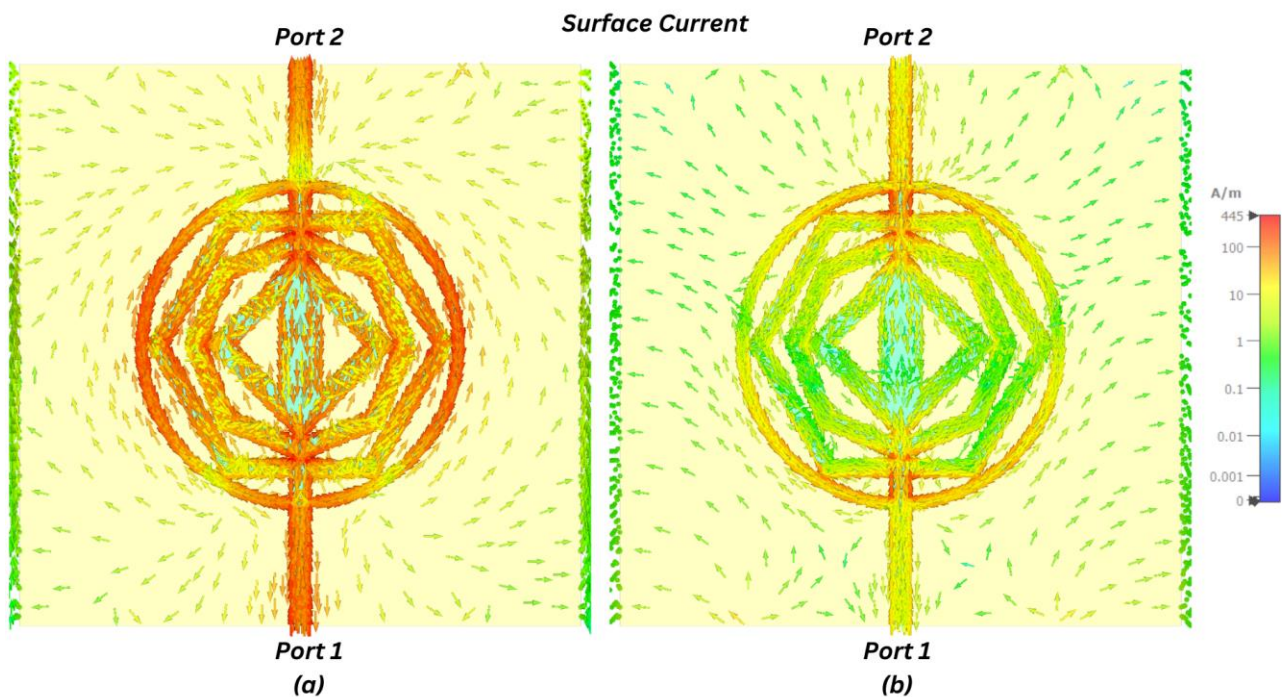


Figure 6. The distribution of surface currents in two modes: (a) reflection at 5.95 GHz and (b) transmission at 3.98 GHz.

The surface current distribution, when port one is active, is shown in Figure 5, which is the suggested sensor. Thanks to the meticulous effort, the currents enhance the sensor's entire electromagnetic responsiveness via circulating resonators within the metamaterial structure. Surface current distribution is influenced by the geometry and configuration of the metamaterial structure, which is an outcome of knowledge and manipulation. Both sensor ports showed similar surface currents when in transmission mode. Port two shows a smaller surface current in reflection mode compared to port one because of the interaction between the metamaterial structure and the applied electromagnetic field.

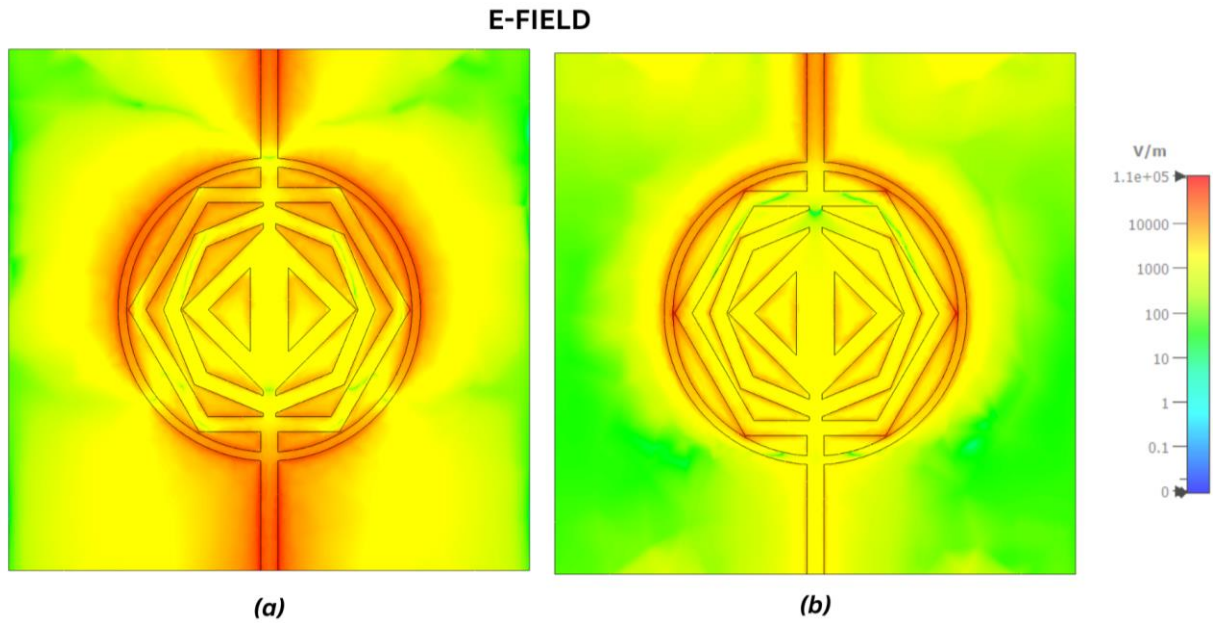


Figure 7. The E-field distribution is illustrated for two modes: (a) S_{21} (transmission coefficient) at 3.98 GHz and (b) S_{11} (Reflection coefficient) at 5.95 GHz.

The functionality of a microwave metamaterial sensor is primarily influenced by the electric field, which is closely tied to the surface current and the S_{11} facilitated by the structure. At a transmission mode(S_{21}) frequency of 3.98 GHz, the sensor exhibits a higher E-field intensity, with comparable intensity levels observed at both ports, indicating efficient signal transmission, as shown in Figure 7(a). Analysis in Figure 7 highlights the resonance mode frequency at 5.95 GHz, characterized by concentrated electric field activity at the sensor's center, particularly in areas of high interaction. The increase in intensity in the field at the activated port, depicted in Figure 7(b), reflects the signal being directed back to the source port. Structure of the metamaterial enhance the ability to confine and concentrate electric fields, resulting in higher intensity at central regions. This electric field plays as a pivotal character in the microwave sensor's environmental responsiveness, significantly affecting its sensitivity to external changes.

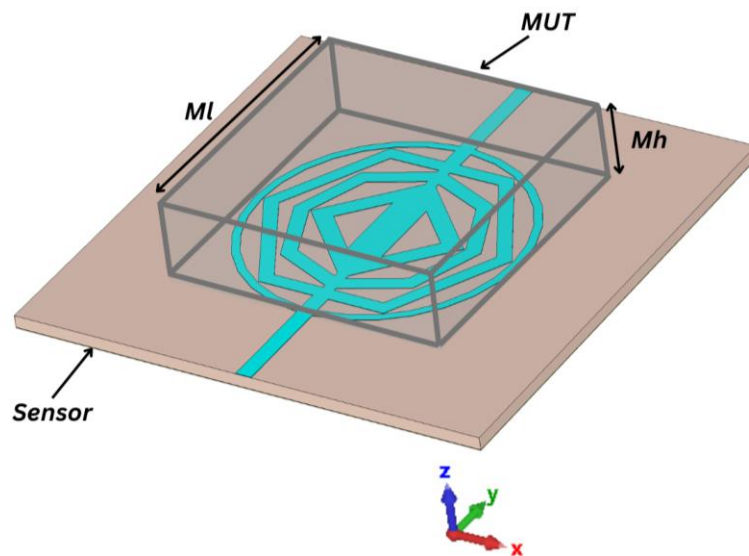


Figure 8. The upper sensor has MUT mounted on it.

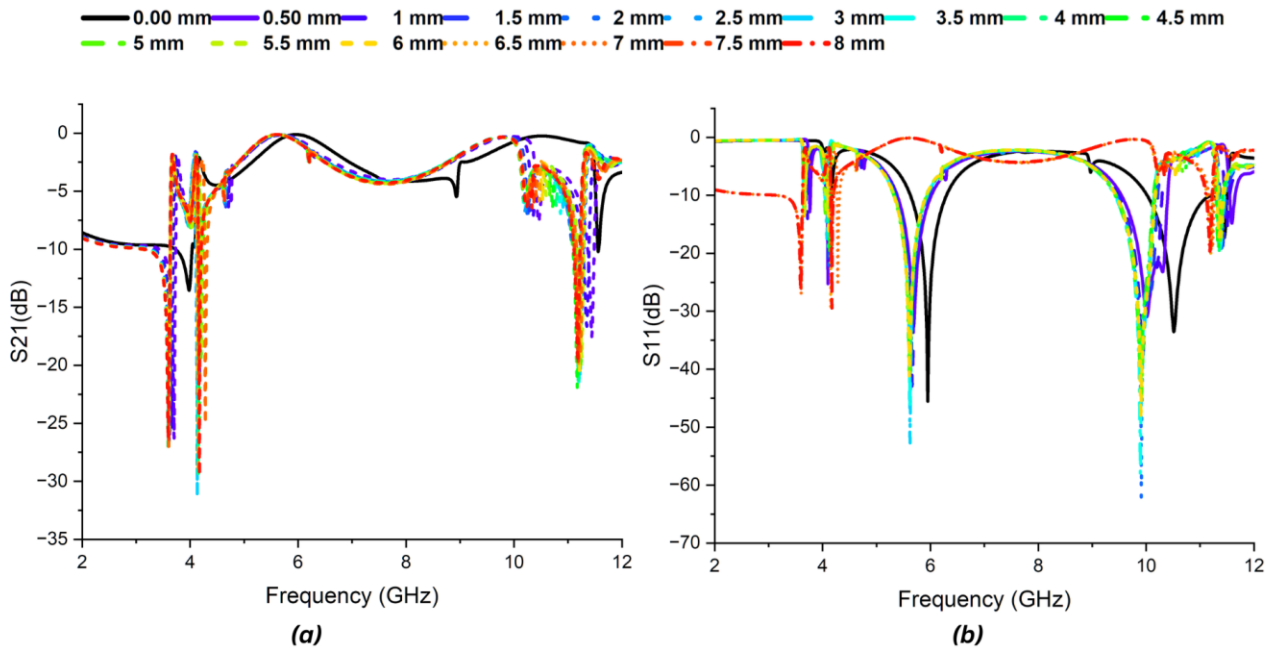


Figure 9. Variation in height of the MUT: (a) S₂₁ and (b) S₁₁ of the sensor.

Table 2. Sensor S₁₁ and S₂₁ resonance peaks at GHz with notch depth.

Thickness (mm)	S ₂₁	dB	S ₁₁	dB
	Freq. (GHz)		Freq. (GHz)	
0.0	3.98	-13.62576	5.96	-46.17994
0.5	3.7	-26.20495	5.69	-45.59792
1.0	3.66	-23.38991	5.66	-42.75295
1.5	3.62	-26.45632	5.64	-47.882
2.0	3.61	-26.45991	5.63	-42.90181
2.5	3.61	-26.61107	5.63	-44.43683
3.0	3.6	-26.76434	5.62	-41.95805
3.5	3.61	-26.17032	5.62	-44.39426
4.0	3.59	-26.86881	5.62	-43.87439
4.5	3.6	-27.02322	5.61	-42.24614
5.0	3.6	-25.78454	5.62	-40.22901
5.5	3.6	-26.48045	5.61	-41.08881
6.0	3.6	-25.99197	5.61	-41.85625
6.5	3.6	-25.83409	5.61	-43.7343
7.0	3.6	-27.0018	5.61	-42.65756
7.5	3.6	-26.48064	5.61	-41.79102
8.0	3.59	-26.34865	5.61,	-39.38103

3. Sensing Result Analysis

The effective engagement of the MUT with the EM fields is a critical factor that influences the sensor's performance. This sensor design utilizes a compact nested hexagonal-shaped resonator, demonstrating

the precision and sophistication of the approach employed. Figure 7 depicts the strategic positioning of the MUT on top of the proposed sensor resonator, with the dimensions of $Ml=17.60$ mm and $Mh=4.8$ mm. The change in the sensor's resonance frequency, observed including and excluding the MUT, forms for the sensitivity of the proposed meta-resonator-based microwave sensor.

The frequency of the sensor (f_s) is influenced by the electromagnetic characteristics of the material under test (MUT). This relationship can be expressed mathematically, indicating that the permittivity, permeability, and volume of the MUT affect the resonance frequency of the sensor, as outlined in equation (1).

$$\frac{\Delta f_s}{f_s} = \frac{\int v(\Delta \epsilon E_1 E_0 + \Delta \mu H_1 H_0) dv}{\int v(\epsilon_0 [E_0]^2 + \mu_0 [H_0]^2) dv} \quad (1)$$

The resonance frequency (Δf_s) is influenced by variations in μ (permeability) and ϵ (permittivity), which are determined by the altered v (volume). In an unperturbed state, the field distributions are represented as E_0 and H_0 , whereas under perturbation, they are denoted as E_1 and H_1 . Changes in the permeability or permittivity of the MUT result in a shift in frequency around the base resonance frequency, as described in Eq. (1). Moreover, as noted in [23], the effects of permeability variations can be neglected for dielectric materials. To maintain resonance, the energies stored of the electric (E) and magnetic (H) fields in the resonator must be balanced. This assumption simplifies Eq. (1), as elaborated in reference [23].

$$\frac{\Delta f_s}{f_s} = \frac{\int v s(\Delta \epsilon E_1 E_0) dv}{\int v(\epsilon_0 [E_0]^2) dv} \quad (2)$$

Table 3. Modeled S_{11} (Reflection) and S_{21} (Transmission) at varying MUT permittivity conditions.

Permittivity	S_{21} (GHz)
1	4.168
2	3.783
3	3.09
4	2.683
5	2.408
6	2.199

The volume is denoted as V_s , which is correlated with the material under test (MUT). Equations (1) and (2) are extensively utilized in cavity resonance techniques and near-field sensors for the analysis and extraction properties of the material [19]. The volume perturbation method adjusts the volume of the MUT by altering its height within a range of 0 to 8 mm. Figure 8 illustrates the impact of these variations on the resonance peaks of the proposed meta-sensor, with the permittivity held constant at 2.2.

The resonance frequencies exhibit a decrease in transmission and reflection modes with an increase in the height of the Material Under Test (MUT). Table 2 displays the relationship between notch depth and resonance frequency for different MUT thicknesses. The resonance frequency shows a shift to lower values, along with an increase in notch depth, due to increased and generated capacitance by the MUT as its v (volume) expands. The capacitance of the MUT remains constant upon reaching a specific height of the MUT, leading to a stable resonance frequency and notch depth. The chosen thickness of 4.8 is identified as the MUT thickness, as at this measurement, the alteration of the resonance frequency is exclusively affected by the permittivity of the MUT. The study examines the effects of changes in permittivity on the resonance peak. The permittivity is adjusted within the range of 0 to 6, assuming that the loss tangent is zero. An increase in permittivity causes the resonance

frequency to shift to a lower value, attributed to the corresponding rise in capacitance, as illustrated in Figure 10.

Table 3 summarizes the permittivity values alongside their resonance frequencies for S_{11} and S_{21} . The data is acquired utilizing established standard dielectric materials, specifically FR-4 ($\epsilon_r = 4.3$), Rogers R04350B ($\epsilon_r = 3.66$) and Rogers RT5880 ($\epsilon_r = 2.2$). These materials are under test (MUT) to assess its sensing performance via the permittivity perturbation technique. Figure 9 illustrates the influence of the microwave sensor, with further details provided in Table 4. The resonance frequency is affected by the minimal thickness of the MUTs, which are all standardized at a height of 1.6 mm. As a result, staking considers a MUT thickness of 4.8. The MUT demonstrates a condition in which its height does not affect the shifting of the resonance frequency. The notch's resonance frequency shifts to a lower value as the relative permittivity of the material under test (MUT) increases.

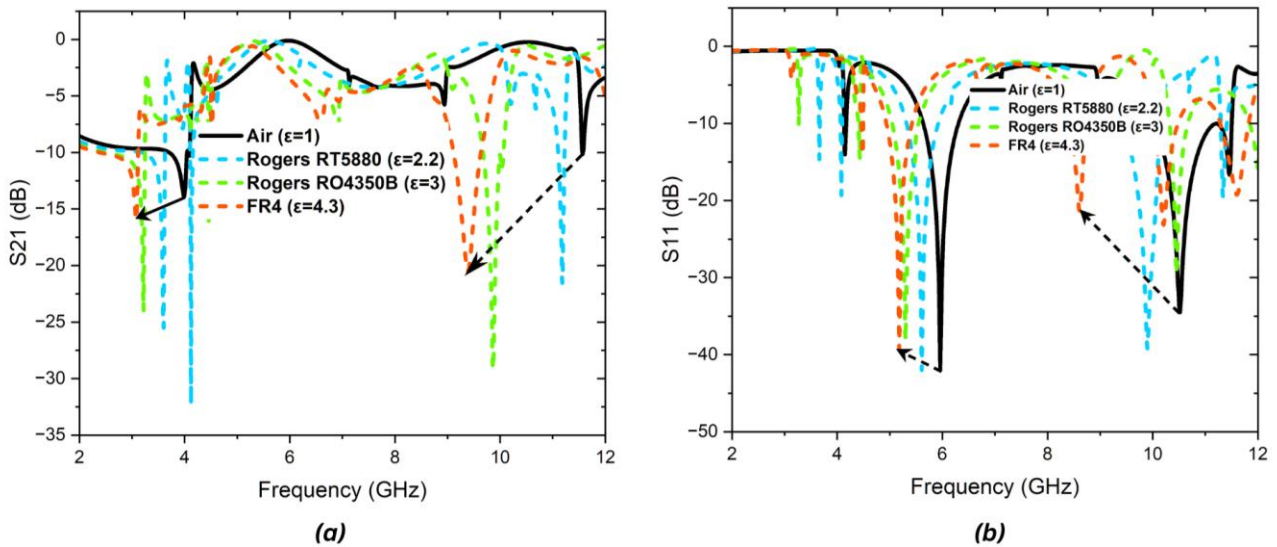


Figure 10. Various permittivity values of MUT were used to simulate (a) S_{11} and (b) S_{21} .

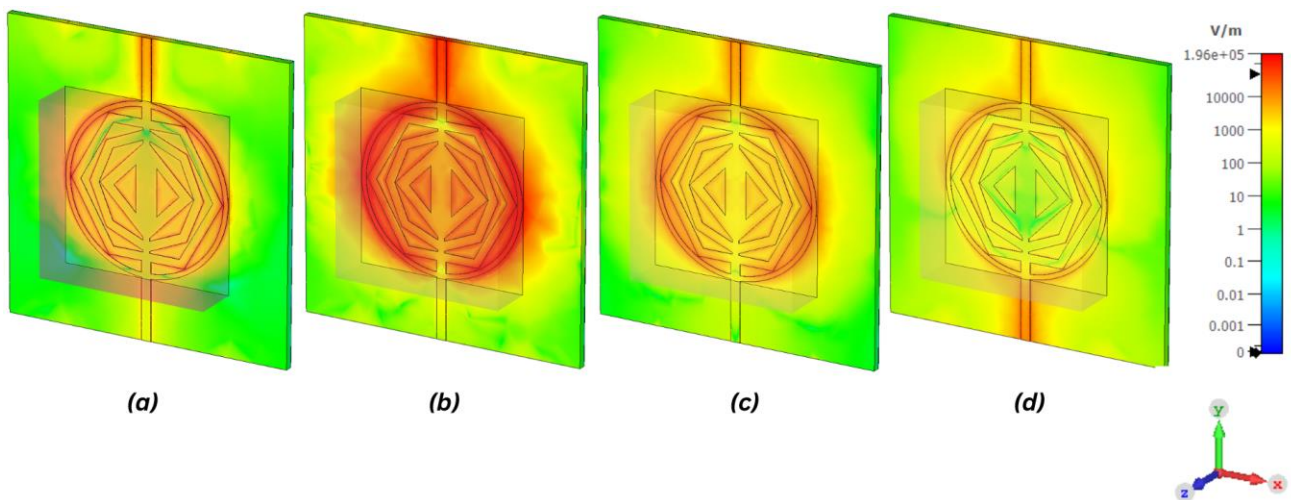


Figure 11. In relation to the MUT, the following is the e-field distribution of the suggested sensor: (a) Air has a resonance peak at 3.99 GHz with an ϵ value of 1, (b) Roger RT5880 has an ϵ value of 2.2 and a peak at 3.6 GHz, (c) Roger RO4350B has an ϵ value of 3.66 and a peak at 3.22 GHz, and (d) FR-4 has an ϵ value of 4.3 and a peak at 3.08 GHz.

The sensitivity of microwave sensors employing permittivity perturbation is defined as the difference ratio in the permittivity of the material under test (MUT) to the corresponding change in the sensor's resonance frequency. Figure 9 depicts the E-field distribution of the proposed sensor at the resonance

peak, along with variations for different MUT samples. The electric field distribution remains uniform at the resonance peak across various measurements, confirming the frequency resonance. The reduced E-field distribution intensity observed for Rogers R04350B and FR-4 indicates a decline in the resonance peak, as shown in Figure 10.

Table 4. S-parameter sensitivity and peak for various standards material under test (MUT).

MUT	Permittivity	S ₂₁	S ₁₁
		Freq. Peak (GHz)	Freq. Peak (GHz)
Air	1	3.99	5.96
Rogers RT5880	2.2	3.6	5.61
Rogers RO4350B	3.66	3.22	5.3
FR-4	4.3	3.08	5.18

The sensitivity of the proposed microwave sensor is a key parameter that determines its ability to detect and respond to environmental changes or variations in the MUT. Several methods are used to evaluate sensitivity in materials. A common approach involves measuring the frequency shift, expressed as ($f_s = f_r - f_0$). In this equation, f_r represents the resonance frequency when the MUT is present, while f_0 indicates the resonance frequency without any load. Changes in the resonance frequencies of microwave meta-sensors reported in the literature make using shifts in frequency as a benchmark for comparison. So, the formula of average sensitivity S_{av} is formed [23].

$$S_{av} = \frac{f_h - f_l}{F_l(\varepsilon_h - \varepsilon_l)} \times 100 \quad (3)$$

The term includes f_h , which denotes the frequency deviation at the maximum μ (permeability), and f_l , which represents the shift in frequency at the minimum μ (permeability), accounting for the effects of μ (permeability). This research considers the condition ($\varepsilon_l = 1$), representing the lowest permittivity. The proposed sensor for assessing its sensitivity utilizes the formula for normalized average sensitivity ($S_{av, f}$), as defined in Eq. (4) [21,24].

$$S_{av, f} = \frac{f_h - f_l}{F_l(\varepsilon_h - \varepsilon_l)} \times 100 \quad (4)$$

This model is dimensionless due to the involvement of frequency. The corresponding results indicate that the relative permittivity of the material under test (MUT) exhibits an inverse relationship with the frequency shift. The sensor's sensitivity, a key determinant of its performance, is inversely related to the increase in the MUT's permittivity. The normalized average sensitivity of the proposed sensor for an alternative standard MUT is 9.55% in transmission mode (S_{21}), as detailed in Table 3. This finding has practical implications, as it demonstrates that the reflection mode, with its greater sensitivity, is the preferred choice for applications involving reflection mode sensing, thereby enhancing the applicability of the proposed sensor.

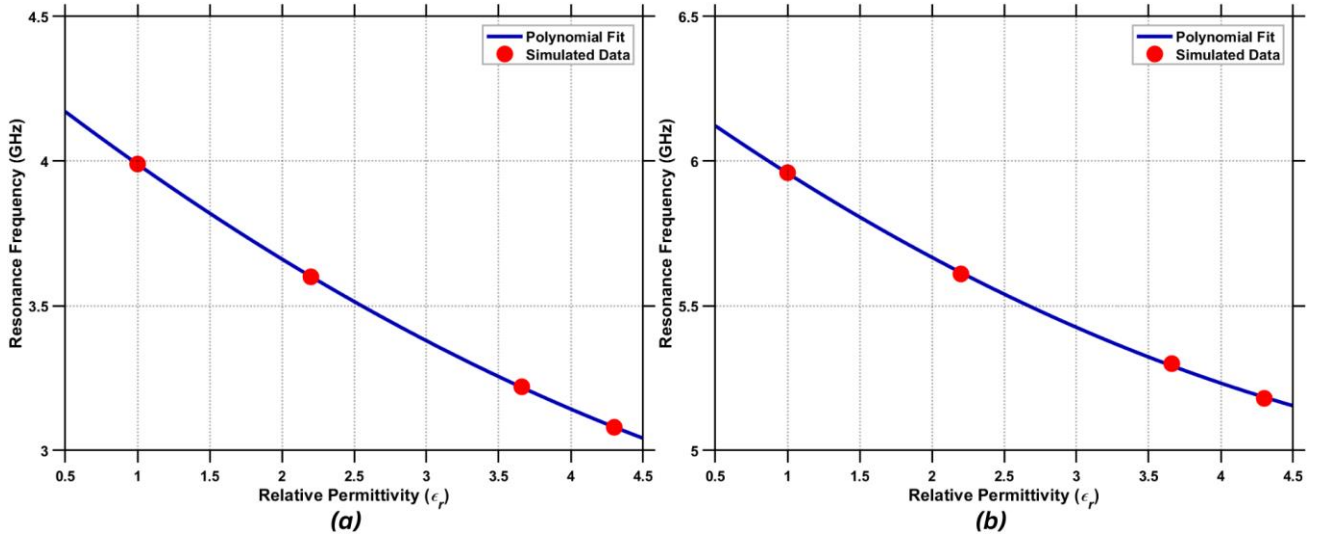


Figure 12. Resonance frequencies of the simulated Transmission and Reflection modes as fitted by the polynomial curves for (a) S_{21} and (b) S_{11} .

4. Analytical Representation of Simulation Results

Polynomial equation

A curve fitting approach has been used to construct a mathematical model to determine the μ (permeability) of materials. Simulated resonance frequencies for few test materials are depicted in Fig. 10, where each symbol represents simulation results, and the solid line reflects the fitted data generated using polynomial equations. To estimate the permittivity (ϵ_r) of the material under test (MUT), a parabolic equation (Eq. (5)) is used during the fitting process [15].

$$f_s(MUT) = X_1 - X_2\epsilon_{r,MUT} + X_3\epsilon_{r,MUT}^2 \quad (5)$$

The equation of polynomial contains constants $X_1, X_2,$ and X_3 , with higher-order terms beyond the third degree excluded because of their very weak role. Figure 11 illustrates that the continuous line begins at f_s (Air) and exhibits a decreasing trend as the permittivity rises. This indicates that when the relative permittivity (ϵ_r) of the material under test (MUT) is 1, the resonant frequency in air (f_s (Air)) acts as the reference point, necessitating that the resonant frequency of the MUT (f_s (MUT)) must match that of f_s (Air). Therefore, the equation is further expanded with $(\epsilon_{r,MUT} - 1)$, where, f_s (Air) denoted as X_1 .

$$f_s(MUT) = X_1 - X_2(\epsilon_{r,MUT} - 1) + X_3(\epsilon_{r,MUT}^2 - 1)^2 \quad (6)$$

Simulations were conducted on well-known dielectric materials, specifically Rogers R04350B, Rogers RT5880, and FR-4. The data obtained and the curve fitting presented in Fig. 11 enabled the determination of the polynomial constants for Eq. (7).

$$f_s(MUT) = 3.99 - 0.3512(\epsilon_{r,MUT} - 1) + 0.0230(\epsilon_{r,MUT}^2 - 1)^2 \quad (7)$$

Table 5. Various MUTs resonance frequencies were computed and simulated.

MUT	Permittivity	S_{21} (GHz)	
		Simulated Peak (GHz)	Calculated Peak (GHz)
Air	1	3.99	3.99
Rogers RT5880	2.2	3.6	3.6017
Rogers RO4350B	3.66	3.22	3.2185

FR-4	4.3	3.08	3.0815
------	-----	------	--------

By incorporating its permittivity, Equation 7 can be utilized to determine the resonance frequency of the well-known MUT. The reflectivity characteristics of the MUT, along with the computed and simulated reflection mode resonance frequencies, are presented in Table 5.

The relative error (RE) is computed using Equation (8).

$$RE = \frac{\text{Simulated_value} - \text{Calculated_value}}{\text{Measured_Value}} \times 100 \quad (8)$$

Table 6. Relative Error between Calculated and Simulated Frequencies.

Permittivity	Relative Error	MUT
1	0.00%	Air
2.2	0.05%	Rogers RT5880
3.66	0.05%	Rogers RO4350B
4.3	0.05%	FR-4

5. Comparison

The suggested sensor demonstrates substantial enhancements relative to previously developed sensors in the table. The compact dimensions of 30×30 mm confer a distinct advantage over more significant configurations, such as the symmetrical split-ring resonator (SRR) in [5], which has measurement of 71.84×68.3 mm, and the dual-hook SRR in [8], which has dimensions of 80×40 mm. Even diminutive designs, such as the rectangular SRR in [11] (35×15 mm) and the complementary splitting resonator (CSRR) in [9] (19×19 mm), fail to achieve the sensitivity and operational performance offered by our work. The utilization of Rogers RT5880 as the substrate material guarantees superior performance characterized by a low-loss tangent and dielectric stability, rendering it similar to the sensors referenced in [5], [6], and [12]. Although the spiral CSRR in [6] employs Teflon as a substrate, which offers low loss properties, the sensitivity of our work (9.55%) much surpasses that of [6] (5.88%). Furthermore, our work provides dual-band functionality at 3.96 GHz and 11.57 GHz inside the S and X bands, augmenting its operational bandwidth. This differs from single-band sensors such as the symmetrical SRR in [5], which functions in the L and S bands, or the magnetic LC resonator in [12], which operates in the S band. Our work achieves a permittivity sensing range of 1–7, which surpasses that of the dual-hook SRR in [8] (2–5.8) and is comparable to the spiral CSRR in [6] (1–6.5). The proposed sensor is appropriate for diverse material characterization applications. The average sensitivity (S_{avg}) of our work at 9.55% markedly exceeds that of other designs, including the CSRR in [9] (3.73%), square DS-CSRR in [10] (4.17%), and rectangle SRR in [11] (5.50%). The proposed sensor significantly surpasses the backbone resonator in [4], attaining a better sensitivity of 6.61% compared to 9.95%. In comparison to alternative designs, such as the complementary curved ring resonator (CCRR) in [13] and the CSRR in [14], which exhibit lower sensitivities of 5.31% and 3.40%, respectively, our work showcases a significant performance improvement. The elevated sensitivity allows the suggested sensor to identify subtle changes in material properties with enhanced accuracy, a crucial attribute for sophisticated applications. Our sensor surpasses other sensors in compactness, sensitivity, frequency range, and permittivity sensing capabilities. It integrates sophisticated design and high-quality materials to position itself as a cutting-edge solution for permittivity characterization in the S and X bands.

Table VII. Assessment of the proposed CNHSR-CRR based sensor in relation to alternative microwave sensors for the characterization of materials under test (MUT).

Ref.	Substrate	Peaks (GHz)	Dimension (mm \times mm)	Permittivity Range	Freq. Band (GHz)	Sensor Type	S_{avg} (%)
[6]	Teflon	3.08, 3.24	N/A	1–6.5	S	CSRR(Spiral)	5.88

[8]	RT/Duroid 6006	2.74, 2.37	80 × 40	2–5.8	S	SRR (Dual Hook)	2.00
[7]	RT/Duroid 6006	2.45	50 × 30	2.09–5.84	S	SRR (Meandered Line)	3.57
[10]	FR-4	4.85	24 × 60	1–4.3	S, C	DS-CSRR	4.17
[9]	Rogers RO4350	2.41	19 × 19	2–10	S	CSRR	3.73
[12]	Rogers RT6002	2.18	N/A	1–10	S	LC	4.03
[11]	RO4003C	5.15	35 × 15	1–5.2	S, C	SRR	5.50
[14]	Rogers RO4350	2.22, 2.46	35 × 26	1–4.4	S, C	CSRR	3.40
[13]	Rogers RO4350	3.49	52 × 34	1–4.4	S	CCRR	5.31
[5]	Rogers RT5880	2.22	71.84 × 68.3	1–4.4	L, S	SRR	1.46
[4]	Rogers RT5880	9.44	30 × 30	1–6	C, X	Backbone resonator	6.61%
This Work	Rogers RT5880	3.96, 11.57	30 × 30	1–6	S, X	CNHSR	9.55%

6. Conclusion

This article presents a novel Compact Nested Hexagonal Metamaterial Sensor that functions inside the S and X-band frequency ranges. The enhanced electromagnetic field is attained using modified nested hexagonal and octagonal closed ring resonators, which amplify electric field strength in the sensing region. This CRR attained a minimal sensor size of 30 mm x 30 mm x 0.79 mm. In the sensor's normal state, the transmission notch occurs at 3.98 GHz and 11.57 GHz, with notch depths of -13.16129 dB and -10.23024 dB, respectively, necessitating a thorough examination of design evolution, parametric analysis, and metamaterial property study. The behaviors of the electromagnetic field are elucidated to comprehend the transmission notch attribute. The resonant frequency alters in response to the Material Under Test (MUT) presence due to electromagnetic field variations. The sensor's sensitivity is examined for known dielectric materials ranging from 1 to 6. The suggested CRR-based sensor attained a remarkable simulated sensitivity of 9.55% in transmission mode (S_{21}) and 9.13% in reflection mode (S_{11}). The compact size and superior sensitivity across the permittivity range of 1 to 6 render the proposed CRR-based sensor a compelling option for solid permittivity sensing applications.

7. References

- [1] R. A. Alahnomi, Z. Zakaria, S. R. Ab Rashid, E. Ruslan, and A. A. M. Bahar, "High-Q sensor based on symmetrical split ring resonator with spurlines for solids material detection," *IEEE Sensors Journal*, vol. 17, no. 9, pp. 2766–2775, May 2017, doi: 10.1109/JSEN.2017.2682266.
- [2] M. S. K. T., M. A. H. Ansari, A. K. Jha, and M. J. Akhtar, "Design of SRR-based microwave sensor for characterization of magnetodielectric substrates," *IEEE Microwave and Wireless Components Letters*, vol. 27, no. 5, pp. 524–526, May 2017, doi: 10.1109/LMWC.2017.2690873.
- [3] M. S. K. T., A. K. Jha, and M. J. Akhtar, "Improved planar resonant RF sensor for retrieval of permittivity and permeability of materials," *IEEE Sensors Journal*, vol. 17, no. 17, pp. 5479–5486, Sep. 2017, doi: 10.1109/JSEN.2017.2724942.
- [4] M. L. Hakim, M. T. Islam, M. S. J. Singh, T. Alam, A. M. Alenezi, and M. S. Soliman, "Intensified electric field-based highly sensitive backbone-shaped C and X band microwave metamaterial sensor

for permittivity characterization applications," *Engineering Science and Technology, an International Journal*, vol. 60, p. 101877, Nov. 2024, doi: 10.1016/j.jestch.2024.101877.

[5] R.A. Alahnomi, Z. Zakaria, E. Ruslan, S.R. Ab Rashid, A.A.M. Bahar, "High-Q sensor based on symmetrical split ring resonator with spurlines for solids material detection," *IEEE Sens. J.*, vol. 17, no. 9, pp. 2766–2775, 2017.

[6] H. Sun, H. Deng, P. Meng, S. Wang, Y. Shuai, Q. Gao, "High-sensitivity sensor loaded with coupled complementary spiral resonators for simultaneous permittivity and thickness measurement of solid dielectric sheet," *IEEE Sens. J.*, vol. 22, no. 23, pp. 22591–22599, 2022.

[7] K.M. Shafi, A.K. Jha, M.J. Akhtar, "Improved planar resonant RF sensor for retrieval of permittivity and permeability of materials," *IEEE Sens. J.*, vol. 17, no. 17, pp. 5479–5486, 2017.

[8] M.S. Kt, M.A.H. Ansari, A.K. Jha, M.J. Akhtar, "Design of SRR-based microwave sensor for characterization of magnetodielectric substrates," *IEEE Microwave Wirel. Compon. Lett.*, vol. 27, no. 5, pp. 524–526, 2017.

[9] Ebrahimi, J. Scott, K. Ghorbani, "Transmission lines terminated with LC resonators for differential permittivity sensing," *IEEE Microwave Wirel. Compon. Lett.*, vol. 28, no. 12, pp. 1149–1151, 2018.

[10] W. Shahzad, W. Hu, Q. Ali, H. Raza, S.M. Abbas, L.P. Ligthart, "A Low-cost metamaterial sensor based on DS-CSRR for material characterization applications," *Sensors*, vol. 22, no. 5, p. 2000, 2022.

[11] Samad, W.D. Hu, W. Shahzad, L.P. Ligthart, H. Raza, "High-precision complementary metamaterial sensor using slotted microstrip transmission line," *J. Sens.*, 2021.

[12] Ebrahimi, G. Beziuk, J. Scott, K. Ghorbani, "Microwave differential frequency splitting sensor using magnetic-LC resonators," *Sensors*, vol. 20, no. 4, p. 1066, 2020.

[13] X. Han, et al., "Microwave sensor loaded with complementary curved ring resonator for material permittivity detection," *IEEE Sens. J.*, vol. 22, no. 21, pp. 20456–20463, 2022.

[14] W.-S. Zhao, et al., "Microwave planar sensors for fully characterizing magneto-dielectric materials," *IEEE Access*, vol. 8, pp. 41985–41999, 2020.

[15] F. Martin, P. Velez, J. Munoz-Enano, L. Su, *Planar Microwave Sensors*, John Wiley & Sons, 2022.

[16] S.R. Shaffer, A. Mahalov, "Permittivity gradient induced depolarization: electromagnetic propagation with the Maxwell vector wave equation," *IEEE Trans. Antennas Propag.* 69 (3) (2020) 1553–1559

[17] M. Navaei, P. Rezaei, "Permittivity measurement of fluidics with high-sensitivity by chandelier form microwave sensor," *Microw. Opt. Technol. Lett.* 66 (1) (2024) e33955.

[18] P.A. Williams, J.R. Lloyd, "Reliability characterization of a low-K dielectric using magnetoresistance as a diagnostic tool," *IEEE Trans. Device Mater. Reliab.* 21 (3) (2021) 431–435.

[19] M. Nelo, T. Vahera, T. Siponkoski, J. Juuti, H. Jantunen, "Ultra-low permittivity ULTCC composite materials," *Appl. Phys. Lett.* 118 (14) (2021).

[20] W. Shahzad, W. Hu, Q. Ali, H. Raza, S.M. Abbas, L.P. Ligthart, "A Low-cost metamaterial sensor based on DS-CSRR for material characterization applications," *Sensors* 22 (5) (2022) 2000

[21] S. Alam, Z. Zakaria, I. Surjati, N.A. Shairi, M. Alaydrus, T. Firmansyah, "Integrated microwave sensor and antenna sensor based on dual T-shaped resonator structures for contact and noncontact characterization of solid material," *IEEE Sens. J.* 23 (12) (2023) 13010–13018.

- [22] X. Liu, D. Zhang, S. Yu, C. Wang, X. Yang, Y. Wang, A dual-band resonator sensor for low permittivity characterization, *IEEE Trans. Instrum. Meas.* 71 (2022) 1–11.
- [23] M.S. Boybay, O.M. Ramahi, Material characterization using complementary split-ring resonators, *IEEE Trans. Instrum. Meas.* 61 (11) (2012) 3039–3046.
- [24] S. Kiani, P. Rezaei, M. Navaei, Dual-sensing and dual-frequency microwave SRR sensor for liquid samples permittivity detection, *Measurement* 160 (2020) 107805.
- [25] Ebrahimi, J. Scott, K. Ghorbani, Differential sensors using microstrip lines loaded with two split-ring resonators, *IEEE Sens. J.* 18 (14) (2018) 5786–5793.
- [26] Hanif, et al., Compact maze-shaped meta resonator for high-sensitive S-band low permittivity characterization, *Sens. Bio-Sens. Res.* 45 (2024) 100655.
- [27] J. Muñoz-Enano, P. Vélez, M. Gil, and F. Martín, ‘Planar Microwave Resonant Sensors: A Review and Recent Developments’, *Applied Sciences*, vol. 10, no. 7, p. 2615, Apr. 2020, doi: 10.3390/app10072615.
- [28] M.L. Hakim, T. Alam, M.T. Islam, H. Alsaif, M.S. Soliman, Polarization-independent fractal square splits ring resonator (FSSRR) multiband metamaterial absorber/artificial magnetic conductor/sensor for Ku/K/Ka/5G (mm-Wave) band applications, *Measurement* 210 (2023) 112545.